AGU PUBLICATIONS

JGR

Journal of Geophysical Research: Atmospheres

RESEARCH ARTICLE
10.1002/2014JD021591

Key Points:
- Significant influences of climate patterns on winter precipitation are analyzed
- The influences from PNA and ENSO on the 1960s drought are analyzed

Correspondence to:
L. Ning,
lning@geo.umass.edu

Citation:
Ning, L., and R. S. Bradley (2014), Winter precipitation variability and corresponding teleconnections over the northeastern United States, *J. Geophys. Res. Atmos.*, *119*, 7931–7945, doi:10.1002/2014JD021591.

Received 31 JAN 2014
Accepted 11 JUN 2014
Accepted article online 16 JUN 2014
Published online 7 JUL 2014

Winter precipitation variability and corresponding teleconnections over the northeastern United States

Liang Ning[1] and Raymond S. Bradley[1]

[1]Northeast Climate Science Center and Climate System Research Center, Department of Geosciences, University of Massachusetts Amherst, Amherst, Massachusetts, USA

Abstract The variability of winter precipitation over the northeastern United States and the corresponding teleconnections with five dominant large-scale modes of climate variability (Atlantic Multidecadal Oscillation, AMO; North Atlantic Oscillation, NAO; Pacific-North American pattern, PNA; Pacific Decadal Oscillation, PDO; and El Niño–Southern Oscillation, ENSO) were systemically analyzed in this study. Three leading patterns of winter precipitation were first generated by empirical orthogonal function (EOF) analysis. The correlation analysis shows that the first pattern is significantly correlated with PNA and PDO, the second pattern is significantly correlated with NAO and AMO, and the third pattern is significantly correlated with ENSO, PNA, and PDO. To verify the physical sense of the EOF patterns and their correlations, composite analysis was applied to the precipitation anomalies, which reproduced the three EOF spatial patterns. Multiple linear regression models generated using indices of all five modes of climate variability show higher explained variances. Composite analyses of geopotential height, sea level pressure, relative humidity, and moisture flux field were performed to find the physical mechanisms behind the teleconnections. When the findings are applied to the extreme drought of the 1960s, it is found that besides a continuous negative NAO pattern, a negative PNA pattern and La Niña conditions also contributed to the drought of winter season by influencing moisture flux and the position of storm tracks. Another case, the 2009/2010 winter with positive precipitation anomalies over the coastal region, is found to be resulted from circulation patterns dominated by major El Niño condition with high-PNA and PDO indices.

1. Introduction

Global mean temperature averaged over land and ocean surfaces shows a significant increase in recent decades, and precipitation has generally increased over land north of 30°N and decreased in the tropics, with substantial increases of heavy precipitation events and droughts in many continental regions [*Dai et al.*, 1998; *Trenberth et al.*, 2007; *Ning and Qian*, 2009]. Based on the simulations of general circulation models (GCMs), this warming will very likely continue with increased precipitation extremes and droughts [*Meehl et al.*, 2007]. According to the Intergovernmental Panel on Climate Change Fifth Assessment Report, there have been likely increases in either the frequency or the intensity of heavy precipitation over North America and Europe since about 1950 [*Hartmann et al.*, 2013]. Over United States, *Kunkel et al.* [2013] find a nationally averaged upward trend in the frequency and intensity of extreme precipitation events. When assessing the flood magnitudes as represented by trends in annual peak river flow for the last century, *Peterson et al.* [2013] find that the magnitudes have been decreasing in the Southwest, while flood magnitudes in the Northeast and north central United States are increasing. *DeGaetano* [2009] indicate that the 2 year return-period precipitation amount in northeastern U.S. increases at a rate of approximately 2% per decade, whereas the change in the 100 year storm amount is between 4% and 9% per decade.

Over the northeastern United States, GCM simulations indicate that annual and winter precipitation will very likely increase, but there is no significant trend in summer precipitation [*Christensen et al.*, 2007; *Ning et al.*, 2012b]. To reduce uncertainties in the projection of future precipitation over the northeastern U.S., it is important to understand the dynamics of precipitation variability, especially for winter precipitation, which is more significantly related to the large-scale synoptic circulation than the other seasons [*Ning et al.*, 2012a]. Many previous studies [e.g., *Hartley and Keables*, 1998; *Kunkel and Angel*, 1999; *Bradbury et al.*, 2003] have shown that winter precipitation over the northeastern U.S. is influenced by several prominent large-scale modes of climate variability, such as the Atlantic Multidecadal Oscillation (AMO) [*Schlesinger and Ramankutty*, 1994], the North Atlantic Oscillation (NAO) [*Wallace and Gutzler*, 1981; *Barnston and Livezey*, 1987], the Pacific-North

American pattern (PNA) [*Wallace and Gutzler*, 1981; *Leathers et al.*, 1991], the Pacific Decadal Oscillation (PDO) [*Mantua et al.*, 1997], and the El Niño–Southern Oscillation system (ENSO) [*Trenberth*, 1997]. For example, *Griffiths and Bradley* [2007] find positive trends in winter extreme precipitation with reduced consecutive dry days over the northeastern U.S. for the period 1961–2000, and their principle components are significantly correlated with PNA. *Curtis* [2008] also indicates that there is an intensification of extreme precipitation events in the Mid-Atlantic region during positive AMO period, because of an anomalous cyclone advecting moisture into this region.

However, the relationships between winter precipitation and large-scale climate variability are not robust, since the correlation coefficients are usually low [*Hurrell*, 1995; *Bradbury et al.*, 2002b; *Archambault et al.*, 2008]. For example, when defining two new indices, a "trough axis index (TAI)" and a "trough intensity index (TII)", *Bradbury et al.* [2002b] found that the TAI is dominated by the NAO and is highly correlated with winter precipitation at inland sites over the northeastern U.S. As well, the authors found that climate variables over the northeastern U.S. are apparently unrelated to the PNA index although PNA is also correlated with the TII. A statistical analysis by *Archambault et al.* [2008] revealed that negative PNA regimes are associated with above-average cool-season northeastern precipitation, while NAO regimes are found to have relatively little influence on the amount and frequency of cool-season northeastern precipitation. *Bradbury et al.* [2002a] also indicated that correlations between the NAO and precipitation are not significant, although NAO and winter streamflow are highly correlated at some sites over New England, suggesting that interrelationships are most significant in the low-frequency spectrum. *Ropelewski and Halpert* [1986] showed that there is no spatially coherent ENSO signal in terms of temperature and precipitation anomalies identified in the northeastern U.S.

The lack of statistically significant relationships may be because regional precipitation itself has complex inherent variability, and several modes of climate variability also have varying influences across the northeast region, making it difficult to recognize their influence over the whole domain. Therefore, in this study, the influences of the NAO, AMO, PNA, PDO, and ENSO on winter precipitation, and the corresponding physical mechanisms, were systemically analyzed for the first time. Empirical orthogonal function (EOF) analysis was first applied to winter precipitation data to extract the different orthogonal spatial patterns. Linear correlation and composite analysis show that different climate indices have significant influences on different precipitation patterns, explaining why the direct correlations between total winter precipitation and individual climate indices (e.g., NAO and ENSO) were not found to be significant in previous studies [e.g., *Bradbury et al.,* 2002a; *Coleman and Rogers,* 2003]. Then, multiple linear regression (MLR) and composite analysis were used to identify the relationships between large-scale modes of climate variability and different precipitation patterns, and also to examine the physical mechanisms that underlie these relationships.

2. Data

The study area includes the entire northeastern U.S., from 36°–50°N and 90°–68°W as shown in Figure 1. Observed monthly precipitation data with high spatial resolution (~12.5 km) for the period 1949–2010 were used in this study. The data over period 1950–1999 are used for EOF analysis, and the data of winter 2009/2010 are used for a case study as a cross validation. We use the data only through 1999 in the EOF analysis, because the data after 1999 do not include Canada, without which the EOF spatial pattern will be inhomogeneous and the results will be confusing. These data are based on the National Oceanic and Atmospheric Administration (NOAA) Cooperative Observation stations, which were gridded to 12.5 km resolution using the synergraphic mapping system algorithm of *Shepard* [1984] and then scaled to match the long-term average of the parameter-elevation regression on independent slopes model precipitation climatology [*Maurer et al.,* 2002]. One potential issue of this approach is the lower quality over the domain with lower station density or shorter records; however, other data sources, e.g., Environment Canada meteorological stations data and Global Precipitation Climatology Project (GPCP) data, are included to increase the reliability of the data set [*Maurer et al.,* 2002].

The standardized monthly NAO index, AMO index, PNA index, NINO3 index (5°N–5°S, 150°–90°W) for the period 1950-1999 are from NOAA's Climate Prediction Center. The monthly PDO index for the period 1950-1999 is from Joint Institute for the Study of the Atmosphere and Ocean of the University of Washington. The winter indices are averaged for December, January, February, and March, as was common in previous

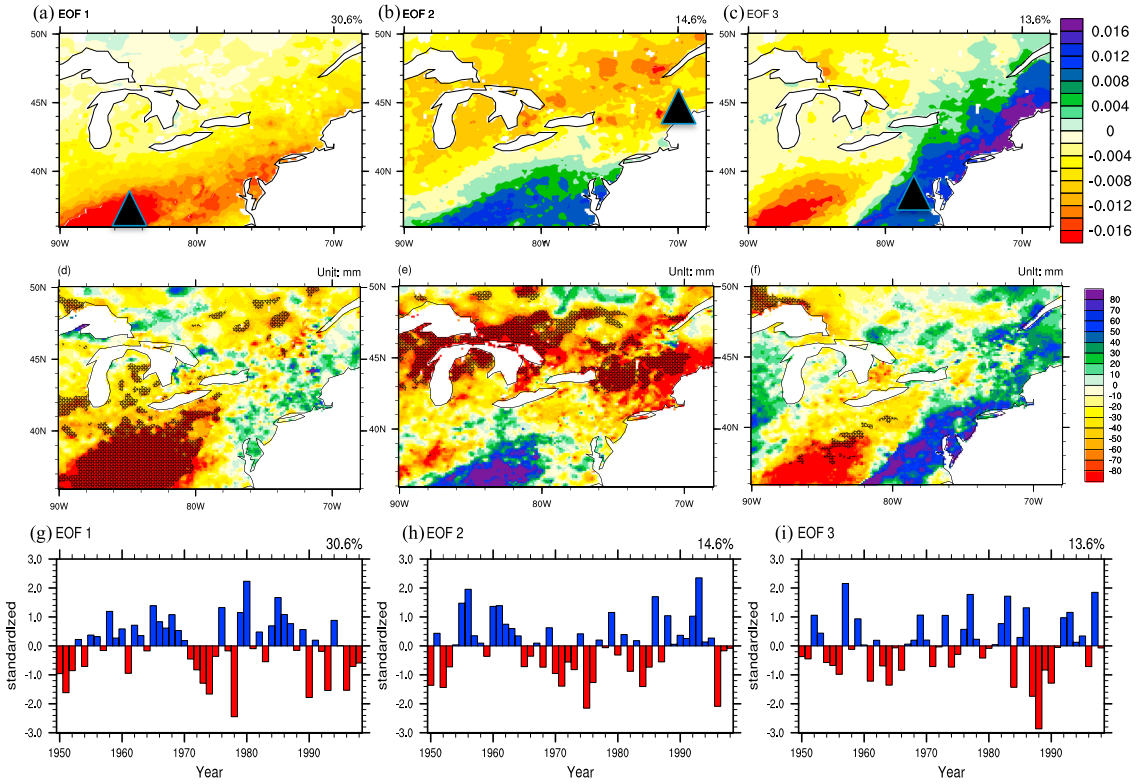

Figure 1. (a–c) The first three EOF spatial patterns, (d–f) reproduction of three EOF spatial patterns through composite analysis on the years shown in Table 2 (unit: mm), and (g–i) the corresponding three standardized EOF time series of winter precipitation over the period 1950-1999. The triangles in Figures 1a–1c show the locations of Greensburg, Gardiner, and Piedmont. Stippled areas in Figures 1d–1f indicate differences that are significant at the 95% level, based on Student t-test.

studies [*Kunkel and Angel,* 1999; *Bradbury et al.,* 2003] because winter conditions usually persist to March over this region, especially over New England. National Center for Environmental Prediction reanalysis data for the period 1950–1999 were used for the monthly gridded 1000 hPa to 500 hPa geopotential heights, *u*- and *v*- components of the wind, relative humidity, specific humidity, and sea level pressure (SLP) fields, with a resolution of 2.5° × 2.5°.

To investigate whether the sample sizes influence the results, a separate observed precipitation data set, the Historical Climatology Network (HCN) version 2.5.0 [*Menne et al.*, 2009], for the period 1900–2007 is also used. The monthly AMO, NAO, NINO3.4, and PDO indices for the period 1990–2007 are also used in the validation. The NINO3.4 index [*Trenberth*, 1997] is from the Climate and Global Dynamics Division of National Center for Atmospheric Research.

3. Methodology

3.1. Empirical Orthogonal Function Analysis

Empirical orthogonal function (EOF) analysis is a widely used statistical technique to reduce a complex data set into linear combinations of fewer new variables, which represent the maximum possible fraction of the variance contained in the original data [*Wilks*, 2006]. Because atmospheric and other geophysical fields generally exhibit many strong connections among the new variables, the EOF method has the potential for yielding substantial insights into the fields' spatial and temporal variations, and new interpretations of the original data can be suggested by the nature of the linear combinations that are most effective in compressing the data [*Wilks*, 2006]. Hence, EOFs have been extensively used to characterize the dominant spatial patterns and the corresponding temporal variability of three-dimensional data sets in atmospheric research [e.g., *Joyce*, 2002]. Therefore, in this study, EOF analysis was first applied to winter precipitation over the northeastern U.S., and the first three patterns, explaining nearly 60% of the total variance, were analyzed.

Table 1. The Correlation Coefficients Between the Time Series of the Three EOF Patterns and Large-Scale Climate Variability[a]

	NAO	AMO	PNA	PDO	NINO3
EOF1	−0.004	−0.07	**0.37**	**0.33**	0.11
EOF2	0.20 ($p = 0.0841$)	**0.24**	0.05	0.07	0.06
EOF3	−0.08	0.01	**0.45**	**0.46**	**0.43**

[a]The bold indicate those significant at 95% level.

3.2. Moisture Flux

The vertically integrated low-level average moisture flux components for winter season were calculated using the following equations [*Coleman and Rogers*, 2003; *Dominguez and Kumar*, 2005]:

$$qu = \frac{1}{g}\int_{1000\ \mathrm{hPa}}^{500\ \mathrm{hPa}} \bar{q}\,\bar{u}\ \mathrm{d}p, \tag{1}$$

$$qv = \frac{1}{g}\int_{1000\ \mathrm{hPa}}^{500\ \mathrm{hPa}} \bar{q}\,\bar{v}\ \mathrm{d}p, \tag{2}$$

where the qu and qv are the zonal and meridional moisture flux components, and $\bar{q}$, $\bar{u}$, and $\bar{v}$ are the seasonal mean specific humidity and zonal and meridional wind components at each pressure level. The two-dimensional moisture flux field was calculated by

$$\vec{\mathrm{q}} = qu\,\vec{\mathrm{i}} + qv\,\vec{\mathrm{j}}, \tag{3}$$

where $\vec{\mathrm{q}}$ is the low-level horizontal moisture flux, and $\vec{\mathrm{i}}$ and $\vec{\mathrm{j}}$ are the unit zonal and meridional vectors.

4. Results

4.1. Winter Precipitation Variability

The first three leading spatial patterns and standardized time series of the winter seasonal average precipitation extracted through EOF analysis are shown in Figures 1a–1c. These three patterns explain 30.6%, 14.6%, and 13.6% of the total variance, respectively, which is typical of many other studies considering the nonlinear component of the precipitation variance [e.g., *Joyce*, 2002; *Wu et al.*, 2005; *Ge et al.*, 2009]. The following three patterns only explain 6%, 4%, and 3% of the total variance, so they are not considered in the study. The first spatial pattern shows a uniformly negative value distribution over the whole domain with larger values over Ohio Valley and the coastal region (Figure 1a). Precipitation over the whole domain shares the same temporal variability on both interdecadal and interannual time scales (Figure 1g). The second EOF shows a north-south pattern with a reversal of sign at ~40°N (Figure 1b), and the corresponding temporal variability is shown in Figure 1h. The third EOF is a coastal-inland pattern, with a positive maximum over the east coast and negative maximum over the Ohio Valley with the border along the Appalachian Mountains (Figures 1c and 1i).

4.2. Relationships With the Large-Scale Climate Variability

The correlation coefficients between the time series of the three leading patterns and the five major large-scale climate indices NAO, AMO, PNA, PDO, and NINO3 are given in Table 1. The first pattern is significantly correlated with PNA and PDO; the second pattern is significantly correlated with AMO, and slightly correlated with NAO ($p = 0.084$); and the third pattern is highly correlated with PNA, PDO, and NINO3. PNA and PDO have totally different influences on EOF1 and EOF3, as these patterns are orthogonal to each other. Notably, although AMO has a period longer than 50 years, it still has strong influence on shorter-scale variation of regional precipitation, and this is also confirmed by previous studies [e.g., *McCabe et al.*, 2004]. Although the correlation coefficients are not very large, they are usually higher than the correlations between the climate indices and winter total precipitation before decomposition shown in previous studies [e.g., *Bradbury et al.,* 2002a; *Coleman and Rogers,* 2003]. Moreover, in the following discussion, when linearly combining the climate indices based on the correlation coefficients, more variance can be explained.

Previous studies show that because of the orthogonality constraint of EOF analysis, sometimes complex and unphysical modes may be produced [*Hannachi*, 2007; *Lian and Chen*, 2012]. Therefore, to demonstrate the physical sense of the three EOF modes and also to verify the correlations between the modes and large-scale

Table 2. The High and Low Index Years of the Three EOF Patterns Used in the Composite Analysis

	High-Index Years	Low-Index Years
EOF1	1960/1961, 1969/1970, 1976/1977, 1977/1978, 1980/1981, 1983/1984, 1985/1986, 1987/1988	1950/1951, 1951/1952, 1954/1955, 1956/1957, 1961/1962, 1964/1965, 1968/1969, 1971/1972
EOF2	1956/1957, 1960/1961, 1998/1999	1968/1969, 1969/1970, 1970/1971, 1976/1977, 1978/1979, 1984/1985
EOF3	1957/1958, 1972/1973, 1982/1983, 1986/1987, 1991/1992, 1997/1998	1955/1956, 1967/1968, 1970/1971, 1973/1974, 1975/1976, 1988/1989

climate variability patterns, the three EOF spatial patterns are reproduced by composting the precipitation anomalies (Figures 1d–1f). The differences of seasonal average precipitation are calculated between the years with high and low climate indices shown in Table 2. A Student's *t* test is applied to examine the significance levels of the composited anomalies. Next, the procedures of selecting years used for the composite for each EOF pattern are discussed in details.

Among the five climate indices, AMO and NAO have the largest correlation coefficients with the second EOF pattern, so we used the years with both high-AMO and high-NAO indices and the years with both low-AMO and low-NAO years to do a composite analysis. To ensure a large enough sample size, the high and low years were defined as those in which both the AMO and the NAO anomalies were ±0.5 standard deviations from the long-term means. The high and low index years of the second EOF pattern are shown in Table 2. Precipitation differences between the high and low climate index years are shown in Figure 1e. The pattern is similar to the second EOF spatial pattern, with negative precipitation anomalies over northern part and positive precipitation anomalies over the southern part of the region.

Because the PNA and PDO influence both the first and third EOF patterns, and the only different factor between the two patterns is the NINO3 index, for the composite analyses of the first EOF pattern, the extremes were defined as both PNA and PDO anomalies ±0.5 standard deviations from their long-term means, but not including those years when the NINO3 index is greater than ±1 standard deviations from the long-term means. This was done to emphasize the influences from PNA and PDO but remove the influence of the NINO3 index. For the composite analyses of the third EOF pattern, to emphasize the influence of the NINO3 index, the extreme years were defined as NINO3 anomalies all greater than ±1 standard deviations from the long-term means. The high and low index years of the first and third EOF patterns are also shown in Table 2. Actually, although the selection for the third EOF pattern is mainly based on NINO3 index, these high-NINO3 and low-NINO3 years also include high- and low-PNA and PDO years. For example, the high-NINO3 years 1982/1983, 1986/1987, and 1997/1998 are also high-PNA and PDO years, and the low-NINO3 years 1955/1956, 1970/1971, 1973/1974, and 1975/1976 are also low-PNA and PDO years. Therefore, although the influences from NINO3 are emphasized at the composite analysis, the influences from PNA and PDO on the EOF3 are also considered. The precipitation differences between the high and low index years for the first and third EOF patterns are shown in Figures 1d and 1f. For the precipitation difference between high-PNA and high-PDO years and the low-PNA and low-PDO years (Figure 1d), the pattern is similar to the EOF1, with obvious negative precipitation anomalies over most regions except some small positive precipitation anomalies over the northern coastal region. For the precipitation difference between high-NINO3 years and low-NINO3 years (Figure 1f), the pattern is similar to EOF3 with an obvious contrast between significant negative precipitation anomalies over the Ohio Valley and significant positive precipitation anomalies over the coastal region. From this, it is clear that the three patterns are fundamental characteristics of winter precipitation regimes across the northeastern U.S.

To verify the relationships between the three patterns and the combinations of these five climate indices, multiple linear regression (MLR) was applied to the three time series. To ensure that maximum observed variance can be explained by the MLR, the climate index with largest correlation coefficient was first selected, and then the following *i*th predictor was selected if the correlation $r_{i,y}$ between it and the predictand met the criterion [*Wilks*, 2006; *Yu*, 2005]:

$$r_{i,y} > r_{i-1,y} \times r_{i-1,i} \tag{4}$$

The coefficients of each large-scale climate mode in the three MLR models are shown in Table 3. From the table, it can be concluded that PNA is the dominant factor in the first pattern of variability, followed by the

Table 3. The Coefficients of Each Large-Scale Climate Variability in the Three Multiple Linear Regression Models

	NAO	AMO	PNA	PDO	NINO3
EOF1	—	—	0.267	0.125	—
EOF2	0.214	0.280	—	0.105	−0.034
EOF3	−0.202	0.049	0.198	0.216	0.256

PDO, while the NAO, AMO, and NINO3 do not contribute to the variability. The AMO and the NAO are the dominant factors in the second pattern of variability, and the PDO and NINO3 contribute far less to the variance. For the third pattern, NINO3, PDO, and PNA are the dominant contributors, and the NAO and AMO contribute much less to the variance. The ranks of these coefficients are consistent with the magnitudes of the correlation coefficients (Table 1), indicating that the MLR models are reasonable combinations of the five climate indices. The MLR models and the three EOF time series are compared in Figure 2. The first MLR model mainly captures the interannual variability and part of the interdecadal variability of the first EOF pattern (Figure 2a). The correlation coefficient between the MLR model and the EOF1 pattern is 0.37, similar to the maximum correlation (0.37) of climate indices and EOF1 and so provides no improvement. The second MLR model mainly captures the interdecadal variability since the AMO is the dominant factor in this model (Figure 2b), with the correlation coefficient (0.34) larger than the maximum correlation (0.24) between the AMO and EOF2. The third MLR model captures the interannual variability of EOF3 with a larger correlation coefficient (0.56) than the maximum correlation (0.46) between the PDO and EOF3 (Figure 2c). Thus, for two of the three MLR models, when the large-scale modes of climate variability are combined, they can explain more variance than any one single climate index.

To confirm that these relationships found over the period 1950–1999 also exist over the longer period, and also that sample size does not influence these results, three stations Greensburg (37.2°N, −85.5°W), Gardiner (44.3°N, −69,8°W), and Piedmont (38.2°N, −78.1°W) with long time series over the period 1900–2007 (from the HCN data) were used to validate the relationships found in the previous discussion. These three stations were selected because they are located at the centers of three EOF patterns (see triangles on Figures 1a–1c). Within the climate indices, the PNA index before 1948 is not available, so it was not used in this analysis. For the same reason, NINO3.4 index instead of NINO3 index was used here. The years after 2007 were not considered because the smoothed AMO data and extended NINO3.4 data were not available after 2007.

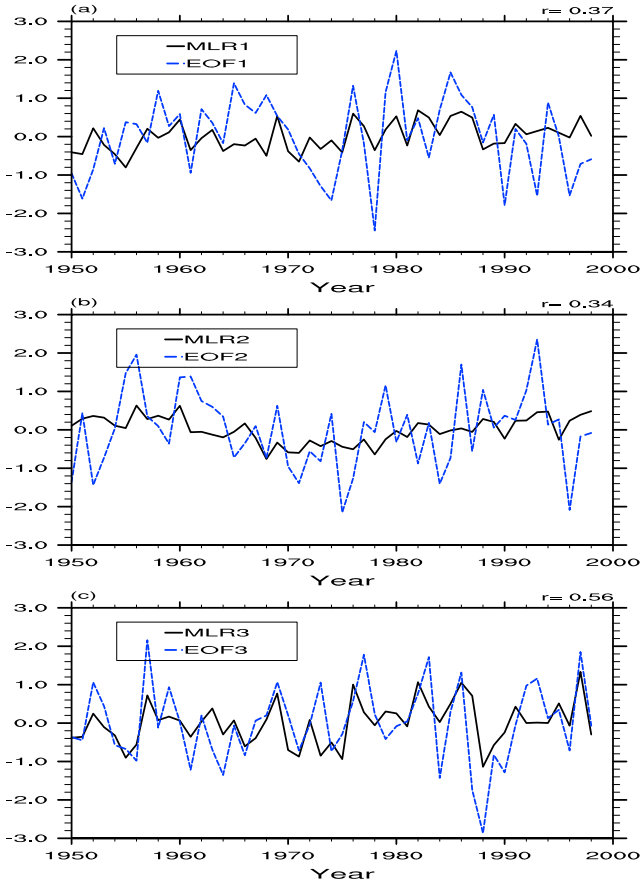

Figure 2. The multiple linear regression models (black) compared to time series of the three patterns (blue): (a) MLR1 versus EOF1, (b) MLR2 versus EOF2, and (c) MLR3 versus EOF3.

The method used in this validation is similar to the method used in Table 2. For the first EOF pattern, the high-PDO years (1 standard deviation above the average) with no ENSO forcing were 1907/1908, 192619/27, 1935/1936, 1969/1970, 1976/1977, 1983/1984, 1985/1986, and 1987/1988, and the low-PDO years were 1917/1918, 1948/1949, 1951/1952, 1956/1957, 1961/1962, 1964/1965, 1968/1969, and 1990/1991. The average monthly precipitation over Greenburg during high-PDO years was 101.7 mm, which is significantly lower than the average 139.1 mm during the

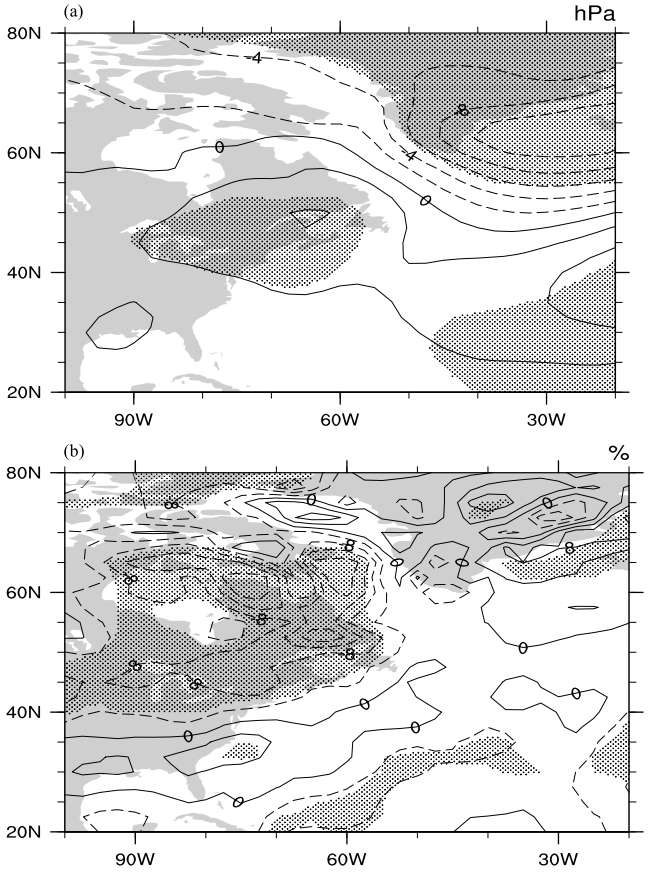

Figure 3. Differences of monthly (a) sea level pressure (unit: hPa) and (b) relative humidity (unit: %) between the high-AMO and high-NAO years and low-AMO and low-NAO years. Stippled areas indicate differences that are significant at the 95% level, based on Student's *t* test.

low-PDO years ($p < 0.05$ based on Student's *t* test). For the second EOF pattern, the high-AMO and NAO years (1 standard deviation above the average) were 1956/1957, 1999/2000, and 2006/2007, and the low-AMO and NAO years were 1916/1917, 1970/1971, 1976/1977, and 1978/1979. The average monthly precipitation over Greenburg during high-AMO and NAO years was 72.9 mm, which is significantly lower than the average 103.6 mm during the low-AMO and NAO years ($p < 0.05$). For the third EOF pattern, the high-NINO3.4 years (1 standard deviation above the average) were 1902/1903, 1905/1906, 1911/1912, 1918/1919, 1925/1926, 1930/1931, 1939/1940, 1940/1941, 1957/1958, 1965/1966, 1968/1969, 1972/1973, 1982/1983, 1986/1987, 1991/1992, 1994/1995, 1997/1998, and 2002/1903, and the low-NINO3.4 years were 1909/1910, 1916/1917, 1933/1934, 1942/1943, 1949/1950, 1950/1951, 1954/1955, 1970/1971, 1973/1974, 1975/1976, 1984/1985, 1988/1989, 1998/1999, and 1999/2000. The average monthly precipitation over Piedmont during high-NINO3.4 years was 83.1 mm, which is significantly higher than the average 68.8 mm during the low-NINO3.4 years ($p < 0.05$). All these three differences are consistent with the EOF patterns and corresponding relationships found in the previous discussion, indicating that sample size does not influence the results.

4.3. Mechanisms Dominating the EOF Patterns

To explain the mechanisms influencing the precipitation EOF patterns, both circulation and humidity fields are used in the following composite analysis. Student's *t* test is applied to examine whether these differences are significant at 95% level. Figure 3a shows the SLP differences between the NAO and AMO high and low years. During the high years, especially because the NAO index is high, there were significant high SLP anomalies over the northern part of the northeastern U.S. with a boundary at ~40°N, which is close to the precipitation difference boundary in the second EOF pattern. Higher pressure acts to block winter storms and thus reduces winter precipitation [*Ning et al.*, 2012b]. This mechanism is also confirmed by the differences of the low-level omega field, which show the vertical velocity (not shown). Since the AMO is defined through the sea surface temperature (SST) over the North Atlantic Ocean, it also reflects an influence on regional precipitation through the water vapor content over the northeastern U.S. When the relative humidity at 850 hPa is calculated, there are significant negative relative humidity anomalies over the northern part of the northeastern U.S., which are associated with less winter precipitation (Figure 3b). Therefore, although NAO and AMO are not correlated ($r = -0.075$), their combined effect is to force negative precipitation anomalies over the northern part of the northeastern U.S. but slightly positive precipitation anomalies over the southern Appalachians.

Both the first and third EOF patterns contain negative centers over the Ohio Valley, but only the third pattern is influenced by the NINO3 index; therefore, this may explain why previous studies found that Ohio Valley winter precipitation is not significantly correlated to the ENSO events [e.g., *Coleman and Rogers*, 2003].

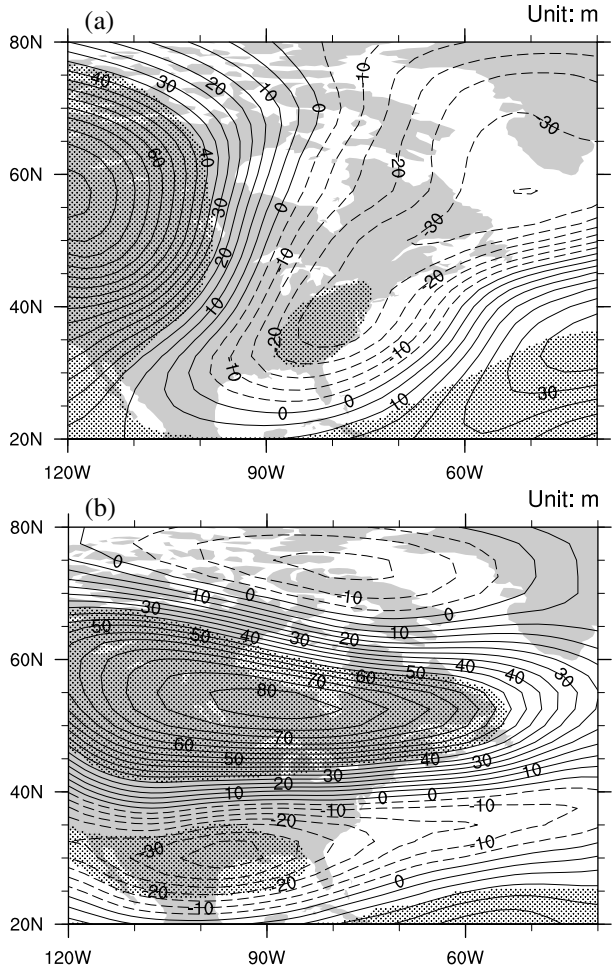

Figure 4. Geopotential height differences of 500 hPa between years with high and low climate mode indices for the (a) first (high-PNA and high-PDO years without ENSO forcing) and (b) third (high-NINO3 year) EOF patterns (m). Stippled areas indicate differences that are significant at the 95% level, based on Student's *t* test.

The PNA, PDO, and ENSO are highly correlated to each other; however, previous studies already showed that the PNA pattern and probability of occurrence are significantly different when tropical Pacific SST anomalies are different [*Straus and Shukla*, 2002]. When there is no ENSO forcing, the 500 hPa geopotential height anomaly field shows a zonal wave train pattern with a positive anomaly centered over the northwestern region of North America and a negative center located over the eastern U.S. (Figure 4a), whereas when there is ENSO forcing, the geopotential height anomalies field shows a meridional wave train pattern with a positive anomaly center located over North America and a negative center located over the southern U.S. (Figure 4b). This is consistent with previous studies that have compared composites of ENSO and PNA and have found that the placement and orientation of high pressure over North America are dramatically different [*Straus and Shukla*, 2000, 2002]. These different circulation patterns induce correspondingly different low-level moisture flux patterns over the northeastern U.S. Moreover, because PDO has similar spatial pattern and temporal variability with ENSO [*Gershunov and Barnett,* 1998; *Newman et al.,* 2003], its influences on the climate over U.S. are also expressed through PNA pattern [*Mantua and Hare,* 2002].

During the high-PNA and high-PDO years without ENSO forcing (Figure 5a), the cyclonic circulation over the southeastern U.S. inhibits the moisture from both the Gulf of Mexico and Atlantic Ocean entering into the northeastern U.S., so there are negative precipitation anomalies over the whole region. In contrast, during high-NINO3 years (Figure 5b), the cyclonic circulation is located further south, so it only inhibits moisture flux from the Gulf of Mexico entering the Ohio Valley but increases moisture transport from the Atlantic Ocean

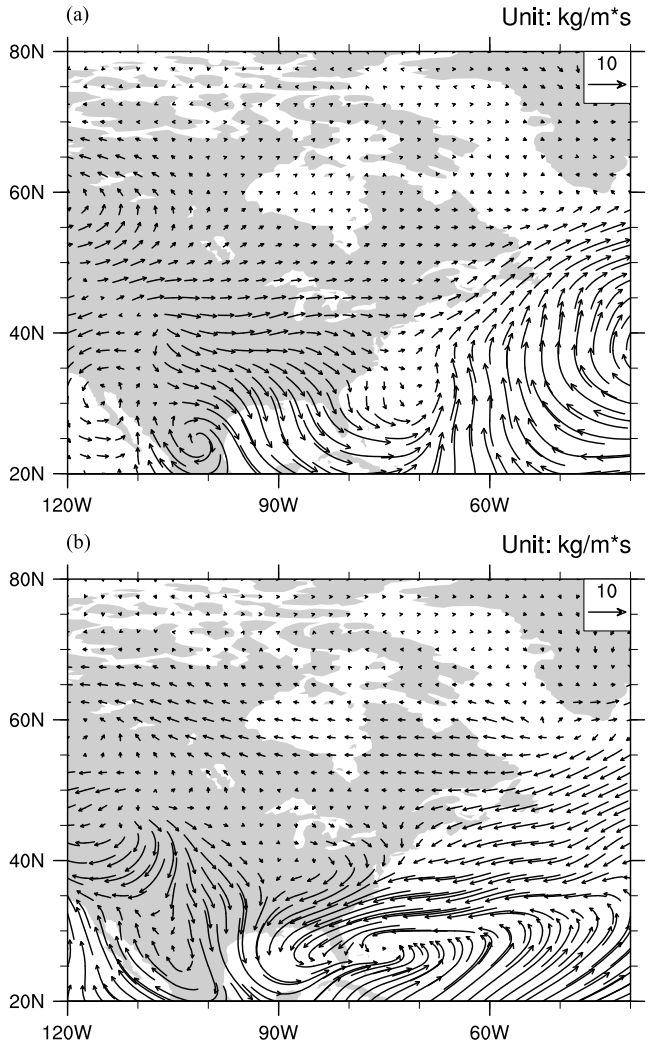

Figure 5. Low-level moisture flux differences between years with high and low climate mode indices for the (a) first (high-PNA and high-PDO years without ENSO forcing) and (b) third (high-NINO3 year) EOF patterns (unit: kg $m^{-1}s^{-1}$).

into the coastal region. Therefore, this moisture flux pattern may result in contrasting precipitation anomalies between the Ohio Valley and the coastal region, which is similar to the third EOF pattern.

Another important factor contributing to the difference between the first and third patterns as a result of ENSO forcing is that during strong El Niño years, there are more winter storms generated in the Gulf of Mexico moving north [*DeGaetano et al.*, 2002], so that there will be more precipitation along the coastal region [*Kunkel and Angel,* 1999; *Hirsch et al.,* 2001]. This theory is confirmed by corresponding SLP differences shown in Figure 6. For the high-PNA and high-PDO years with ENSO forcing (Figure 6b), there are significant negative SLP anomalies over Gulf of Mexico and along the coastal region, indicating a higher possibility of winter cyclone development. Hence, positive precipitation anomalies locate along the coastal region in the east of Appalachian Mountains, similar to the third EOF pattern, during strong El Niño years. In contrast, for those high-PNA and high-PDO years without ENSO forcing (Figure 6a), there is no such SLP anomaly pattern indicating a uniform precipitation anomaly pattern similar to the first EOF pattern.

5. Case Studies

5.1. The 1960s Drought

A severe drought occurred in the early to mid-1960s over the northeastern U.S., significantly influencing the fresh water supply and imposing severe damage on the environment and agriculture across the region

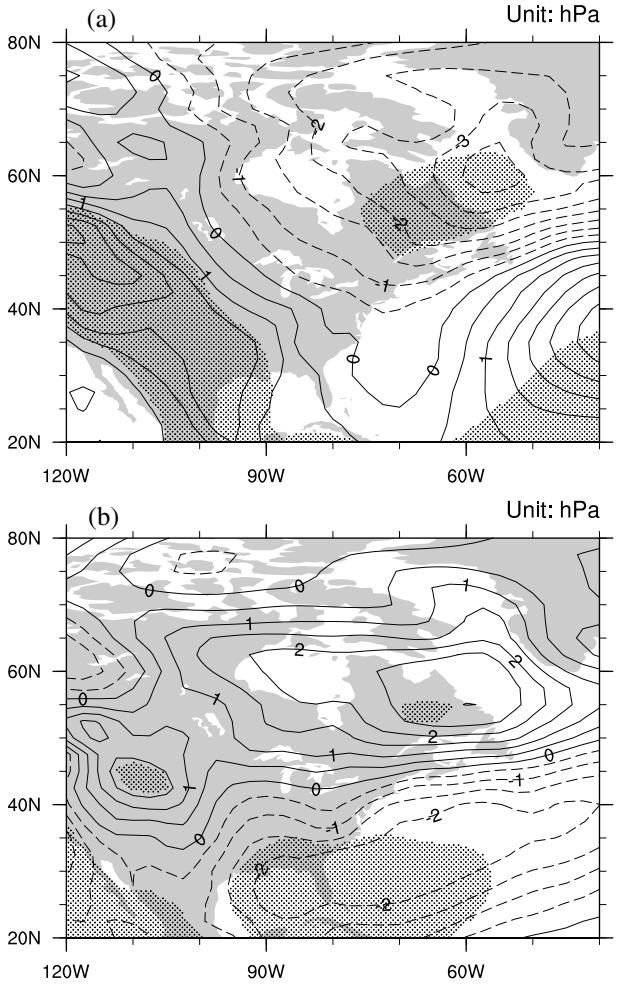

Figure 6. SLP differences between years with high and low climate mode indices for the (a) first (high-PNA and high-PDO years without ENSO forcing) and (b) third (high-NINO3 year) EOF patterns (unit: hPa). Stippled areas indicate differences that are significant at the 95% level, based on Student's *t* test.

[*Bradbury et al.*, 2002a; *Seager et al.*, 2012]. *Namias* [1966] attributed this drought to anomalously cold surface water along the continental shelf, accentuating atmospheric baroclinicity along the eastern boundary of the cold water and providing a source for low-level cooling (increased static stability) of air arriving ahead of cold fronts, thereby inhibiting precipitation over the land areas. *Bradbury et al.* [2002a] suggested that persistent negative NAO conditions might have contributed to the severity of the 1960s drought through exceptionally cool regional air temperatures, low SSTs, and unique regional storm track patterns. *Seager et al.* [2012] also concluded that in winter and spring, the 1960s drought was associated with a low-pressure anomaly over the midlatitude North Atlantic Ocean and northerly subsiding flow over the greater Catskill region that would likely have suppressed precipitation. They also pointed out that the SST anomalies were not the cause of the drought but were forced by northerly flow anomalies. *Barlow et al.* [2001] also found that the northeastern drought of the 1960s was closely linked to the SST anomaly of North Pacific mode, which induced a cyclonic circulation over the East Coast opposing the moisture transportation over the continent from the Gulf Coast to the Northeast. According to *Seager et al.* [2012], the drought happened in all four seasons; however, in this study, since we mainly focus on winter precipitation variability, the physical reasons for the winter contribution to the 1960s drought will be discussed.

Based on our EOF analysis, this persistent drought is displayed in all three patterns (Figures 1g–1i), indicating that the 1960s drought was the result of complex climate variability, rather than involving one single factor. When linearly combining the three EOF patterns, we would expect the most severe drought to have occurred

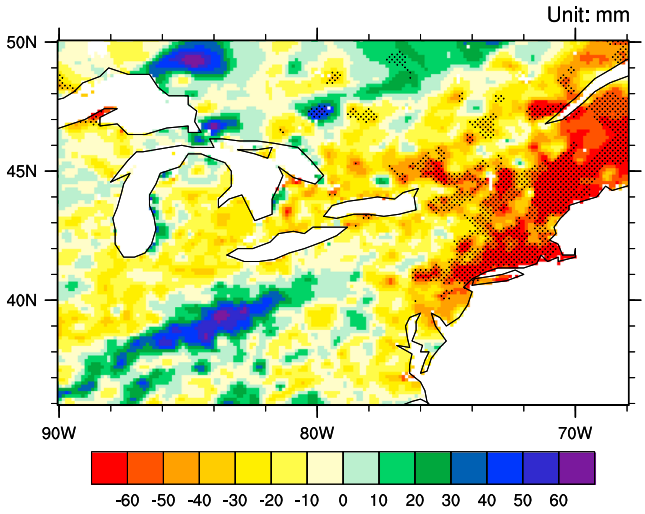

Figure 7. Observed winter precipitation anomalies during the period 1961/1962–1965/1966 (unit: mm). Stippled areas indicate differences that are significant at the 95% level, based on Student's *t* test.

over the northeast part of this region, and this is consistent with the observed precipitation anomalies (Figure 7). To find the additional mechanisms responsible for the 1960s drought, we focus on the third EOF pattern, which has the highest correlation coefficient with the climate indices in the MLR analysis. Another reason to choose the third pattern is that previous studies mainly attributed the mechanism of the drought to NAO [e.g., *Bradbury et al.*, 2002a; *Seager et al.*, 2012], while the contributions from PNA and ENSO were rarely discussed.

During the 1961/1962–1965/1966 winter, the tropical Pacific was mainly under weak La Niña conditions and the PNA index ranged mainly from −1 to −0.5, indicating that the meridional wave train pattern was reversed so that there was a negative 500 hPa geopotential height anomaly over the middle and western section of the U.S. with no distinct circulation pattern over the southeastern U.S. (Figure 8a). Moreover, because there was also a negative geopotential height anomaly over the Atlantic Ocean due to the persistent negative NAO conditions (Figure 8a), the 500 hPa prevailing wind over the eastern U.S. was strongly from the West (Figure 8b), inhibiting moisture transport from either the Gulf of Mexico or the Atlantic Ocean. This resulted in minimal moisture flux over the northeastern U.S. during this period (Figure 8c), which contributed to the severity of the drought. In addition, during La Niña winters, there is no significant increase in the number of winter storms from the Gulf of Mexico influencing the east coast region as in El Niño winters [*Hirsch et al.*, 2001; *Frankoski and DeGaetano*, 2011], and this prevented relief of the drought from winter precipitation. These results indicate that although PNA and ENSO were not dominant factors influencing the 1961/1962–1965/1966 winter drought, they still contributed to the severity of the drought.

5.2. The 2009/2010 Winter

To do a cross validation of the EOF analysis, the 2009/2010 winter, which is out of the EOF analysis period, was selected as a case study. The 2009/2010 winter was characterized as a major El Niño year [*Yu et al.*, 2012] with high-PNA index (larger than 1 standard deviation) and high-PDO index (larger than 0.5 standard deviation). Although the data over Canada are not available, the spatial pattern of precipitation anomalies (Figure 9a) is similar to the third EOF pattern (Figure 1c), and this is consistent with relationship shown in section 4.2.

The corresponding patterns of SLP (Figure 9b) and low-level moisture flux (Figure 9c) are also similar to the patterns of the composited with high-PNA and high-PDO years with ENSO forcing (Figures 5b and 6b). The SLP gradient over the east coast of U.S. indicates a larger possibility of precipitation over the coastal region of the northeastern U.S. The moisture flux anomalies prevent the moisture transport from the Gulf of Mexico to the Ohio Valley, so there are negative precipitation anomalies over Ohio Valley. Moreover, there are above-average numbers of winter storms generated along the east coast region because of the El Niño conditions (http://ecws.eas.cornell.edu/strong_forecast.html), and this also contributes to more precipitation over the coastal region of the northeastern U.S.

6. Conclusions

The lack of a significant relationship between winter precipitation over the northeastern U.S. and large-scale modes of climate variability are addressed in this study. Winter precipitation was decomposed into three principle patterns through EOF analysis, and then the influences of the three patterns from these five modes were examined. The first EOF pattern (30.6% of total variation) showed uniform distribution over the whole

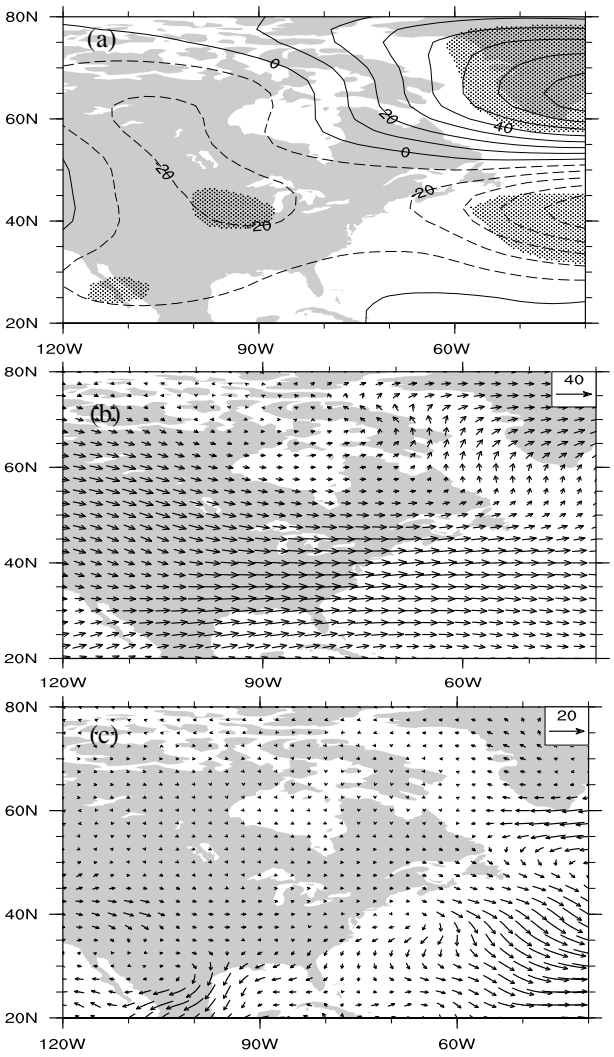

Figure 8. The anomalies of the (a) 500 hPa geopotential height (unit: m), (b) 500 hPa wind field (unit: m/s), and (c) low-level moisture flux (unit: kg $m^{-1}s^{-1}$) during the period 1961/1962–1965/1966 winter. Stippled areas in Figure 8a indicate differences that are significant at the 95% level, based on Student's *t* test.

region with larger values over the Ohio Valley and the east coast region, and was significantly correlated with PNA and PDO indices. The second EOF pattern (14.6% of total variation) showed the contrast between the northern part and the southern part of the region, with a boundary at ~40°N, and was significantly correlated with AMO and NAO indices. The third EOF pattern (13.6% of total variation) showed a contrast between the coastal and inland regions, with the boundary along the Appalachian Mountains, and was significantly correlated with PNA, PDO, and NINO3 indices.

These relationships and the physical senses of the three EOF patterns were confirmed by composite analysis of the precipitation differences and a multiple linear regression of the five indices. Multiple regression models, within which the weight of each index is consistent with its correlation with each EOF pattern, can usually explain higher variances of the EOF patterns than a single index.

The composite analyses were applied to SLP, relative humidity, 500 hPa geopotential height, and moisture flux fields to investigate the mechanisms influencing the three EOF patterns. For the second EOF pattern, during the high-NAO and high-AMO years, there were significant positive SLP anomalies and negative relative humidity anomalies over the northern part of the northeastern U.S., both of which resulted in negative precipitation anomalies. For the first EOF pattern, without ENSO forcing, the 500 hPa geopotential height anomalies field inhibits the moisture from both the Gulf of Mexico and Atlantic Ocean entering into the northeastern U.S., so there are uniform negative precipitation anomalies over the whole region. By contrast, during high-NINO3 years, there is anomalous moisture flux from the Atlantic Ocean to the coastal region, and this is different from the high-PNA and high-PDO years. Moreover, the significant negative SLP anomalies over the Gulf of Mexico and the coastal region correspond to increased winter storms generated from the Gulf of Mexico during El Niño years, which may also have contributed to the contrast between the positive precipitation anomalies over the coastal region and negative precipitation anomalies over the inland region.

Two case studies were then examined to validate the mechanisms and also show how these mechanisms can help understand the variability of regional winter precipitation over the northeastern U.S. The first case is the early to mid-1960s winter drought. The composite 500 hPa geopotential height field for the period 1961/1962–1965/1966 winter shows that there were negative anomalies over the U.S. and Atlantic Ocean due to negative PNA and NAO conditions, and this resulted in strong low-level westerlies over the whole region. The westerly wind anomalies inhibited the moisture flux from both the Gulf of Mexico and the Atlantic Ocean, contributing to the severity of the drought, and the below-average number of winter storms during weak La Niña conditions also prevented any relief from this drought.

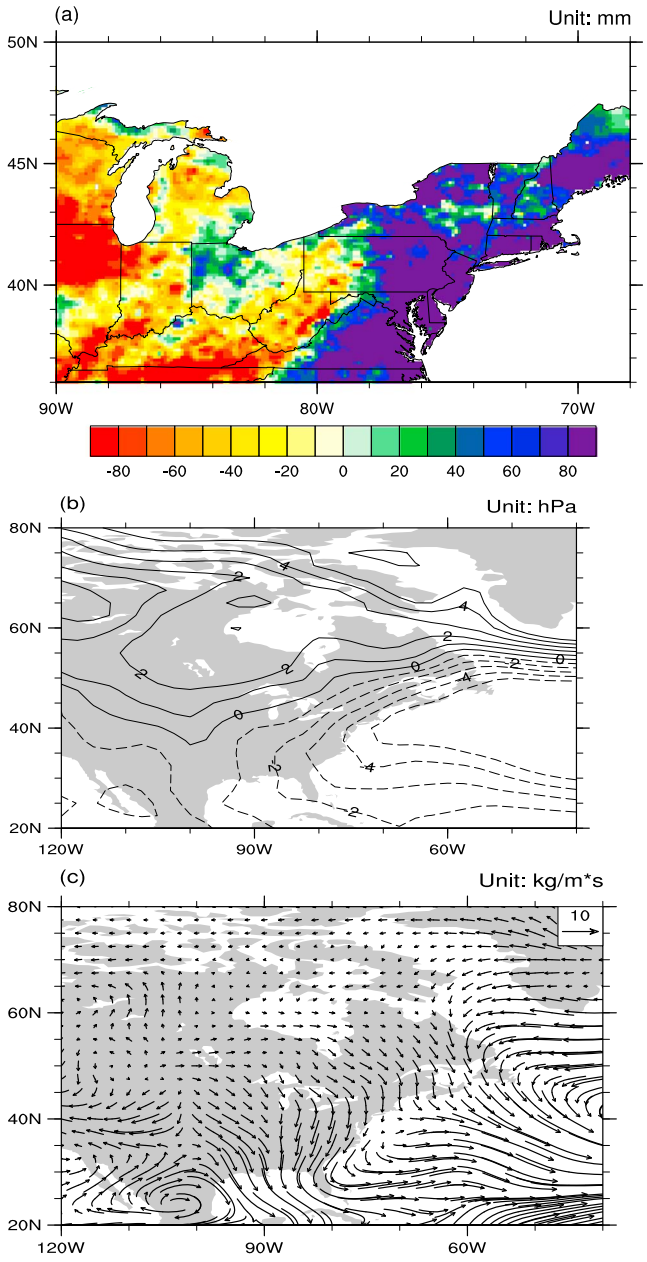

Figure 9. The anomalies of the (a) precipitation (unit: mm), (b) SLP (unit: hPa), and (c) low-level moisture flux (unit: kg $m^{-1}s^{-1}$) during the period 2009/2010 winter.

Another case study of the 2009/2010 winter, which was characterized as positive precipitation anomalies over the coastal region and negative precipitation anomalies over the inland region similar to the third EOF pattern, resulted from major El Niño conditions with high-PNA and high-PDO indices. The SLP gradient and low-level moisture flux anomalies were similar to composites for the third EOF pattern. Moreover, the above-average number of winter storms along the east coast also contributed to these positive precipitation anomalies.

These findings of significant relationships between three component of winter precipitation and five large-scale modes of climate variability, and the corresponding mechanisms, can improve our understanding of winter precipitation over the northeastern U.S. These relationships can also help reduce uncertainties in projections of future regional precipitation.

Acknowledgments
This research was supported by the Department of Interior's Northeast Climate Science Center, under USGS funding G12AC00001. Edwin P. Maurer (Santa Clara University) kindly provided the observation data. The AMO, NAO, PNA, NINO3 time series, and the NCEP grid data were obtained from The National Centers for Environmental Prediction (NCEP). The PDO time series data was made available by the Joint Institute for the Study of the Atmosphere and Ocean (JISAO) of the University of Washington. The extended NINO3.4 index was made available by the Climate and Global Dynamics Division (CGD) of National Center for Atmospheric Research (NCAR). The HCN monthly data were obtained from National Climatic Data Center (NCDC) of National Oceanic and Atmospheric Administration (NOAA).

References

Archambault, H. M., L. F. Bosart, D. Keyser, and A. R. Aiyyer (2008), Influence of large-scale flow regimes on cool-season precipitation in the northeastern United States, *Mon. Weather Rev.*, *136*, 2945–2963.

Barlow, M., S. Nigam, and E. H. Berbery (2001), ENSO, Pacific decadal variability, and U.S. summertime precipitation, drought, and stream flow, *J. Clim.*, *14*, 2105–2128.

Barnston, A. G., and R. E. Livezey (1987), Classification, seasonality, and persistence of low-frequency atmospheric circulation patterns, *Mon. Weather Rev.*, *115*, 1083–1126.

Bradbury, J. A., S. L. Dingman, and B. D. Keim (2002a), New England drought and relations with larger scale atmospheric circulation patterns, *J. Am. Water Resour. Assoc.*, *38*, 1287–1299.

Bradbury, J. A., B. D. Keim, and C. P. Wake (2002b), U.S. east coast trough indices at 500 hPa and New England winter climate variability, *J. Clim.*, *15*, 3509–3517.

Bradbury, J. A., B. D. Keim, and C. P. Wake (2003), The influence of regional storm tracking and teleconnections on winter precipitation in the Northeastern United States, *Ann. Assoc. Am. Geogr.*, *93*, 544–556.

Christensen, J. H., et al. (2007), Regional climate projections, in *Climate Change 2007: The Physical Science Basis*, edited by S. Solomon et al., pp. 847–940, Cambridge Univ. Press, Cambridge, U. K., and New York.

Coleman, J. S., and J. C. Rogers (2003), Ohio River Valley winter moisture conditions associated with the Pacific-North American teleconnection pattern, *J. Clim.*, *16*, 969–981.

Curtis, S. (2008), The Atlantic multidecadal oscillation and extreme daily precipitation over the US and Mexico during the hurricane season, *Clim. Dyn.*, *30*, 343–351.

Dai, A., K. E. Trenberth, and T. R. Karl (1998), Global variations in droughts and wet spells: 1900–1995, *Geophys. Res. Lett.*, *25*, 3367–3370, doi:10.1029/98GL52511.

DeGaetano, A. T. (2009), Time-dependent changes in extreme-precipitation return-period amounts in the continental Untied States, *J. Appl. Meteorol. Climatol.*, *48*, 2086–2099.

DeGaetano, A. T., M. E. Hirsch, and S. J. Colucci (2002), Statistical prediction of seasonal east coast winter storm frequency, *J. Clim.*, *15*, 1101–1117.

Dominguez, F., and P. Kumar (2005), Dominant modes of moisture flux anomalies over North America, *J. Hydrometeorol.*, *6*, 194–209.

Frankoski, N. J., and A. T. DeGaetano (2011), An East Coast winter storm precipitation climatology, *Int. J. Climatol.*, *31*, 802–814.

Ge, Y., G. Gong, and A. Frei (2009), Physical mechanism linking the winter Pacific-North American teleconnection pattern to spring North America snow depth, *J. Clim.*, *22*, 5135–5148.

Gershunov, A., and T. P. Barnett (1998), Interdecadal modulation of ENSO teleconnections, *Bull. Am. Meteorol. Soc.*, *79*, 2715–2725.

Griffiths, M. L., and R. S. Bradley (2007), Variations of twentieth-century temperature and precipitation extreme indicators in the northeast United States, *J. Clim.*, *20*, 5401–5417.

Hannachi, A. (2007), Pattern hunting in climate: A new method for finding trends in gridded climate data, *Int. J. Climatol.*, *27*, 1–15.

Hartley, S., and M. J. Keables (1998), Synoptic associations of winter climate and snowfall variability in New England, USA, 1950–1992, *Int. J. Climatol.*, *18*, 281–298.

Hartmann, D. L., et al. (2013), Observations: Atmosphere and surface, in *Climate Change 2013: The Physical Science Basis. Contribution of Working Group I to the Fifth Assessment Report of the Intergovernmental Panel on Climate Change*, edited by T. F. Stocker et al., pp. 159–254, Cambridge Univ. Press, Cambridge, U. K., and New York.

Hirsch, M. E., A. T. DeGaetano, and S. J. Colucci (2001), An east coast winter storm climatology, *J. Clim.*, *14*, 882–899.

Hurrell, J. W. (1995), Decadal trends in the North Atlantic Oscillation: Regional temperature and precipitation, *Science*, *269*, 676–679.

Joyce, T. M. (2002), One hundred plus years of wintertime climate variability in the eastern United States, *J. Clim.*, *15*, 1076–1086.

Kunkel, K. E., and J. R. Angel (1999), Relationship of ENSO to snowfall and related cyclone activity in the contiguous United States, *J. Geophys. Res.*, *104*, 19,425–19,434, doi:10.1029/1999JD900010.

Kunkel, K. E., et al. (2013), Monitoring and understanding trends in extreme storms: State of knowledge, *Bull. Am. Meteorol. Soc.*, *94*, 499–514.

Leathers, D. J., B. Yarnal, and M. A. Palecki (1991), The Pacific/North American teleconnection pattern and United States climate. Part I: Regional temperature and precipitation associations, *J. Clim.*, *4*, 517–528.

Lian, T., and D. Chen (2012), An evaluation of rotated EOF analysis and its application to tropical Pacific SST variability, *J. Clim.*, *25*, 5361–5373.

Mantua, N. J., and S. R. Hare (2002), The Pacific Decadal Oscillation, *J. Oceanogr.*, *58*, 35–44.

Mantua, N. J., S. R. Hare, Y. Zhang, J. M. Wallace, and R. C. Francis (1997), A Pacific interdecadal climate oscillation with impacts on salmon production, *Bull. Am. Meteorol. Soc.*, *78*, 1069–1079.

Maurer, E. P., A. W. Wood, J. C. Adam, D. P. Lettenmaier, and B. Nijssen (2002), A long-term hydrologically-based data set of land surface fluxes and states for the conterminous United States, *J. Clim.*, *15*(22), 3237–3251.

McCabe, G. J., M. A. Palecki, and J. L. Betancourt (2004), Pacific and Atlantic Ocean influences on multidecadal drought frequency in the United States, *Proc. Natl. Acad. Sci. U.S.A.*, *101*, 4136–4141.

Meehl, G. A., et al. (2007), Global climate projections, in *Climate Change 2007: The Physical Science Basis*, edited by S. Solomon et al., pp. 747–845, Cambridge Univ. Press, Cambridge, U. K., and New York.

Menne, M. J., C. N. Walliams, and R. S. Vose (2009), The United States Historical Climatology Network monthly temperature data—Version 2, *Bull. Am. Meteorol. Soc.*, *90*, 993–1007.

Namias, J. (1966), Nature and possible causes of the northeastern United States drought during 1962–1965, *Mon. Weather Rev.*, *94*, 543–554.

Newman, M., G. P. Compo, and M. A. Alexander (2003), ENSO-forced variability of the Pacific Decadal Oscillation, *J. Clim.*, *16*, 3853–3857.

Ning, L., and Y. Qian (2009), Interdecadal change of extreme precipitation over South China and its mechanism, *Adv. Atmos. Sci.*, *26*, 109–118.

Ning, L., M. E. Mann, R. Crane, and T. Wagener (2012a), Probabilistic projections of climate change for the mid-Atlantic region of the United States—Validation of precipitation downscaling during the historical era, *J. Clim.*, *25*, 509–526.

Ning, L., M. E. Mann, R. Crane, T. Wagener, R. G. Najjar, and R. Singh (2012b), Probabilistic projections of anthropogenic climate change impacts on precipitation for the mid-Atlantic region of the United States, *J. Clim.*, *25*, 5273–5291.

Peterson, T. C., et al. (2013), Monitoring and understanding changes in heat waves, cold waves, floods, and droughts in the United States: State of knowledge, *Bull. Am. Meteorol. Soc.*, *94*, 821–834.

Ropelewski, C. F., and M. S. Halpert (1986), North American precipitation and temperature patterns associated with the El Niño/Southern Oscillation (ENSO), *Mon. Weather Rev.*, *114*, 2352–2361.

Schlesinger, M. E., and N. Ramankutty (1994), An oscillation in the global climate system of period 65–70 years, *Nature*, *367*, 723–726.

Seager, R., N. Pederson, Y. Kushnir, J. Nakamura, and S. Jurburg (2012), The 1960s drought and the subsequent shift to a wetter climate in the Catskill Mountains Region of the New York City watershed, *J. Clim.*, *25*, 6721–6742.

Shepard, D. S. (1984), Computer mapping: The SYMAP interpolation algorithm, in *Spatial Statistics and Models*, edited by G. L. Gaile, C. J. Willmott, and D. Reidel, pp. 133–145, Springer Press, Dordrecht, Netherlands.

Straus, D. M., and J. Shukla (2000), Distinguishing between the SST-forced variability and internal variability in mid latitudes: Analysis of observations and GCM simulations, *Q. J. R. Meteorol. Soc.*, *126*, 2323–2350.

Straus, D. M., and J. Shukla (2002), Does ENSO force the PNA?, *J. Clim.*, *15*, 2340–2358.

Trenberth, K. E. (1997), The definition of El Niño, *Bull. Am. Meteorol. Soc.*, *78*, 2771–2777.

Trenberth, K. E., et al. (2007), Observations: Surface and atmospheric climate change, in *Climate Change 2007: The Physical Science Basis*, edited by S. Solomon et al., pp. 235–336, Cambridge Univ. Press, Cambridge, U. K., and New York.

Wallace, J. M., and D. S. Gutzler (1981), Teleconnections in the geopotential height field during the Northern Hemisphere winter, *Mon. Weather Rev.*, *109*, 784–812.

Wilks, D. S. (2006), *Statistical Methods in Atmospheric Sciences,* 2nd ed., 648 pp., Academic Press, Burlington, MA, San Diego, and London.

Wu, A., W. W. Hsieh, and A. Shabbar (2005), The nonlinear patterns of North American winter temperature and precipitation associated with ENSO, *J. Clim.*, *18*, 1736–1752.

Yu, J.-Y. (2005), Geoscience data analysis—Regression and objective analysis. [Available at http://www.ess.uci.edu/~yu/class/ess210b/lecture.3.regression.all.pdf.]

Yu, J.-Y., Y. Zou, S. T. Kim, and T. Lee (2012), The changing impact of El Niño on US winter temperatures, *Geophys. Res. Lett.*, *39*, L15702, doi:10.1029/2012GL052483.